Amorphous titanium-oxide supercapacitors with high capacitance

doi: 10.1209/0295-5075/128/58001

Amorphous titanium-oxide supercapacitors with high capacitance

M. Fukuhara,[1,a)] T. Kuroda,[1] F. Hasegawa,[1] Y. Shirai,[1] T. Suwa,[1] T. Hashida,[2] and M. Nishijima[3]

[1] *New Industry Creation Hatchery Center, Tohoku University, Aoba, Sendai, Japan 980-8579*

[2] *Fracture and Reliability Research Institute, Graduate School of Engineering, Tohoku University, Sendai, Japan, 980-8579*

[3] *The Electron Microscopy Center, Tohoku University, Aoba, Sendai, 980-8577, Japan*

PACS 84.32.Tt − Capacitors

PACS 78.55.Qr – Amorphous materials; glasses and other disordered solids

PACS 61. 46.-w – Structure of nanoscale materials

* Corresponding author. *E-mail:* fukuhara@niche.tohoku.ac.jp (M. Fukuhara)

Abstract − An amorphous titanium-oxide film oxidized anodically on amorphous Ti-10at%V-15at%Si alloy ribbons demonstrated superior electric properties; remarkable increase in parallel capacitance *Cp*, series capacitance *Cs*, time constant *RCs*, and decrease in dielectric loss with decreasing frequency. The oblate semicircle after a semicircle with a Warburg region in a Nyquist diagram and rapid increases in the real impedance at the lower−frequency region in the Bode diagram demonstrate a parallel circuit comprising electric transport resistance, *Re* (0.64 MΩ), and a higher electric double layer capacitance, C_{dl} (604.0 μF/cm^2) at a nanometer-sized (~53 nm in convex size) uneven surface between a (Ti, V) oxide layer ~ 45 nm deep and air.

Introduction. − A significant amount of scientific and technological research on the storage of electrical energy has been reported since the 1990 [1-6]. Chemical and material researcher have focused on power source devices such as batteries and fuel

cells over the past three decades. In addition to the devices above, the most popular electrochemical capacitor is the electric double-layer capacitor (EDLC) where the interfaces of high specific-area materials such as porous carbon materials or the porous metal oxides of some metals are charged and discharged by ion or radical diffusion [3, 5, 6]. Generally, a dc battery and an ac capacitor are separated for the practical use of electric storage. The ability to store charge for both dc and ac applications would results in significant advancements in electronic devices and electric power applications. Recently, we found that amorphous titanium-oxides (ATOs) and aluminum-oxides (AAOs), indicating *RC* constant larger than that of the EDLC [7] and a switching effect of positive and negative electricity from the atmosphere [8], respectively, can be regarded as a dc/ac converting device with nanometer-sized uneven surfaces [9, 10].

In anticipation of higher capacitances, we reported a Ti−Ni−Si amorphous alloy supercapacitor,[9] constructed using a distributed constant-equipment circuit with large resistance and small capacitance on an amorphous TiO_{2-x} surface containing many 50−70 nm cavities with a higher work function of 5.5 eV [11] that can illuminate a red LED for 37 ms after being charged with 1 mA at 10 V[9]. These materials store ac electricity from 193−453 K with a voltage variation between 10−150 V and a dc capacitance of ~4.8 F (~52.8 kF/cm^3). A typical requirement for electric storage is a surface with nanometer-sized cavities and high electrical resistance. The amorphous materials of interest are completely different from the conventional “wet” cells, such as EDLCs and secondary cells, which are controlled through ion diffusivity. We termed this device a “dry” electric distributed constant capacitor (EDCC) [7-11]. In this study, Ti−V−Si alloys were chosen as starting alloys for the formation of passive oxide films with nanometer-sized uneven structures using a valve metal of vanadium to obtain larger capacitance compared to that of Ti−Ni−Si alloys [7-9, 11].

Experiments. − Ti-10at%V-15at%Si alloy ingots (compositions given in nominal atomic percentage) were prepared by arc-melting mixtures of Si (99.999 % purity), Si (99.999 % purity), and V (99.9 % purity) in an argon atmosphere purified by Ti-gettering. Ribbon specimens of 50−μm thick and 1−mm wide were prepared from the ingots by the rapid solidification of the melt on a single copper roller in a He atmosphere at a tangential velocity of 52.3 m/s, using a single-wheel melt-quenching apparatus (NEV-A05-R10S, Nisshin Giken).

Subsequent anodic oxidation of the specimens were performed for 3.6 ks in 0.4 M H_2SO_4 at 60 V and 278 K. The ample structure of the anodic oxidized specimens was examined at 40 kV by X-ray diffraction (XRD) in the reflection mode with

monochromatic Cu Kα radiation. The surface morphologies were analyzed by atomic force microscope (AFM: SPA400 SII Nano Technology) using a tapping scan mode for a scanning window of $0.5 \times 0.5\ \mu m^2$ with $512^x \times 256^y$ measurement points.

After preparing TEM specimens by focused ion beam (FIB; Quanta 3D Dual Beam system, Themo Fisher Scientific)) using the lift-out method, the depths of the layers were determined from the elemental mapping of Ti, V, Si, and O by Scanning Transmission Electron Microscope (STEM) with an aberration-corrected TEM (Titan³ G2 60-300 Probe Corrector, Themo Fisher Scientific) at 200 kV.

After applying a silver coat of 0.5 mm in diameter on a specimen (1−mm wide, 40 −μm thick, and 10−mm long) with double-oxidized surfaces, the specimen was sandwiched directly by two copper ribbons beneath two pieces of glass plates using a clamp. The capacitance of the specimen was measured using galvanostatic charge/discharge on a potentiostat/galvanostat (SP-150, BioLogic Science) at frequencies between 1 mHz and 1 MHz under a constant voltage of 10 mV at room temperature. All electronic measurements were performed in an Al shield box, to prevent the electromagnetism of the environment.

Results and discussion. − Because a small amount of Ni remained in the amorphous oxide layer that was anodically oxidized on Ti−Ni−Si amorphous alloys [11], we used amorphous Ti−V−Si alloys to form rigid passive oxide films for this study. Because the electric capacitance of ATOs increases proportionally to the negative sixth power of the convex diameter *d*, up to 7 mF/cm^2 [9], we used the anodic polarization method to form a nanometer-sized uneven surface. The current-time curve anodically oxidized at 60 V is shown in fig. 1(a), along with that of Ti-10at%V-15at%Si one at 50 V. Although both curves are characterized by continuous spark-discharging behaviors for the formation of uneven oxide surfaces [12, 13], the curve of the former stabilized at 0.01 mA/cm^2, while the latter curve increases gradually with anodization time. This clearly demonstrates the passivation of the oxide film in the former by the usage of valve metal, V. The XRD pattern (fig. 1(a), inset) can be regarded as a Ti-based amorphous alloy coated with amorphous titanium oxide layers, as well as anodically oxidized Ti-15at%Ni-15at%Si alloys [7]. The primary broad peak (~39° in 2θ) is different from those (~29° and ~24° in 2θ) of amorphous vanadium [14] and silicon [15] oxides, respectively. Figure 1(b) shows a three-dimensional AFM topography image of the surface structure for the anodically oxidized Ti−V−Si and Ti−Ni−Si amorphous specimens, exhibiting an uneven surface with ~53 nm in convex showing uneven surface as well as in Ti-Ni-Si one [12]. However, the depth (~1 nm) of the sunken location of the former is more shallow than

that (~82 nm) of the latter. From High angle Annular Dark-Field Scanning TEM (HAADF-STEM) images and the elemental mapping of Ti, V, Si, and O in fig. 1(c), we observed two layers; upper (Ti, V) oxide of depth 45 nm, and lower (Ti, Si) oxide of depth 80 nm on the Ti−V−Si alloy. The former would be a rigid passive oxide. The reason for formation of the (T, V) oxide film will be described in another paper.

To analyze the electrostatic contribution of the specimen nondestructively, we measured the ac impedance from 1 mHz to 1 MHz in the Nyquist and Bode diagrams at room temperature. A complex-plane (Nyquist) plot of the impedance data is shown in fig. 2(a). The alloy's impedance variation with frequency followed the combined pattern of a line slope of $\pi/4$ rad and two semi circles, an almost semitrue circle with a lower resistance, and an oblate circle with a higher resistance. The $\pi/4$−rad region (Warburg regions) is a consequence of distributed resistance/capacitance in porous electrode [16, 17]. This suggests that the electrode is an ATO film with a porous surface of higher resistance. A reactance, R, of 0.64 (1.36−0.74) MΩ and a relaxation time, RC_{total}, of 75.73 s at the top of the oblate semicircle were derived from the formula $RC_{\text{total}} = 1/(2\pi f_{max})$, where f_{max} (= 2.1 mHz) is the peak frequency. Thus, the total capacitance of the specimen, C_{total}, was calculated to be 54.93 μF (604.0 μF/cm^2). This value is 24 times larger than that (~25 μF/cm^2) [18] of the conventional supercapacitor. If the R and specific surfaces of the ATO increase, the C_{total} of the ATO will increase even more. Figure 2(b) shows the frequency dependence on the real and imaginary impedances. A rapid increase is shown in the real impedance compared with the imaginary impedance in the lower-frequency region. Moreover, the capacitive behavior (near the 0 rad phase angle) in the frequency region between 100 and 0.001 Hz (fig. 2(c)) is clear evidence of a parallel-RC circuit. Thus, ATO films with a nanometer-sized uneven surface between (Ti, V) oxide and air offer an electric distributed constant structure for enhancing electric capacitance. Furthermore, because the shallow valleys in fig. 1(d) improve charge/discharging characteristics at higher frequencies [19], it would not be desirable for solid-state supercapacitors to exhibit a high-aspect-ratio nanotube structure on the ATO [7]. An ATO with a nanometer-sized uneven surface could not be realized using crystalline titanium-based alloys, but could be realized using amorphous alloys [20].

We can store electricity in ac using a rectifier. The series and parallel capacitances, and RCs and RCp time constants in an applied voltage of 10 V at room temperature are presented in fig. 3(a), as a function of frequency. Both capacitances increase exponentially with decreasing frequency. The total capacitance C_{total}, 54.93 μF (604.0 μF/cm^2) at the top (1.378 MΩ, 2.1 mHz) of the oblate semicircle in fig. 2(a) is approximately 0.045 and 125.8 times for Cs and Cp at 2.1 mHz in fig. 3(a), respectively.

This difference suggests a parallel−series combined circuit for the specimen used in this study. The *RCs* increase parabolically in all frequency regions with decreasing frequency, while *RCp* increases parabolically from 1 MHz to 1 kHz and saturates from 1 kHz to 10 Hz, and subsequently increases up to approximately 10 s again parabolically. The 3.4 ks and 9.8 s at 1 mHz are 680,000 and 2,000 times larger than that (5 ms) in the conventional EDLC [21], respectively. A larger duration from 0.1 s to a few hours is required for practical use.

A liquid-phase capacitor such as an aluminum electrolyte capacitor generates leak current by parallel or series resistance through dc, resulting in an apparent enhancement in capacitance. To clarify the enhancement in capacitance accompanied by the decrement in frequency, we calculated the frequency-dependent dielectric loss, tan δ, and series and parallel resistances *Rs* and R_e. These results are shown in fig. 3(b). With decreasing frequency, tan δ shows one peak at approximately 0.24 Hz and subsequently decreases close to zero, while *Rs* and R_e increase from approximately 140 and 30 kHz, respectively, saturates from 1 to 0.2 Hz, and subsequently increases rapidly. The reason for the 0.24-Hz peak is still unclear. These results impose severe constraints in the possibility that capacitance enhancement in series and parallel circuits is caused by the leak current of the capacitor in lower-frequency regions. Although the dielectric loss of 16.3 at 1 mHz is large, the dc capacitance could be increased considerably.

Finally, we consider the origin of the higher-capacitance ATO. Figure 4(a) shows an equivalent circuit with two semicircles corresponding to the Nyquist diagram in fig. 2(a). Because the ATO with oxygen vacancies is characterized by electronic conduction [9] the equivalent circuit corresponding to the oblate semicircle can be recognized by a parallel circuit comprising electric transport resistance, *Re* and electric double layer capacitance, C_{dl} at the uneven surface between the solid film and air [16]. Figure 4(b) shows a schematic representation of a possible mechanism for the large electrical charges observed at the microscopic level. In an uneven surface with nanometer-sized cavities of ATO, electric double layers are formed at the electrically negative concave portion/air interfaces. This is a capacitor with an electric distributed-constant circuit as well as the EDLC. These results indicate the potential for further advances in the fabrication of amorphous titanium dioxide supercapacitors by enhancing a specific surface and integrating oxide ribbons in a micro-electromechanical system.

REFFERENCES

[1] WINTER M. and BRODD, R. J., *Chem. Rev.*, **104** (2004) 4245.
[2] WHITTINGHAM, M., *MRS Bull.*, **33** (2008) 411.

[3] CONWAY, B. E. in *Electrochemical Supercapacitors: Scientific Fundamentals and Technological Applications* (Plenum Press, New York, 1999).

[4] SIMON, P and GOGOTSI, Y., *Nature Mat*., **7** (2008) 845.

[5] ARICÓ, A. S., BRUCE, P., SCROSATIV, B., TARASCON, J. M. and SCHALKWIJK, W., *Nature Mat*., **4** (2005) 366.

[6] EL-KADYI, M. F., STRONG V. DUBIN, S. and KANER, R. B., *Science,* **335** (2012) 1326.

[7] FUKUHARA M. and SUGAWARA, K., *Nanoscale Res. Lett*., **9** (2014) 253.

[8] FUKUHARA, M., KURODA, T., HASEGAWA, F., HASHIDA, T., KWON, E. and KONNO, K., *Europhys. Lett.,* **123** (2018) 58004.

[9] FUKUHARA, M., KURODA, T. and HASEGAWA, F., *Sci. Rep.,* **6** (2016) 35870.

[10] FUKUHARA, M., KURODA, T., HASEGAWA, F., Shirai, Y., Hashida, T. and Konno, K., *J. Alloy. Comp.*, **776** (2019) 757.

[11] FUKUHARA M. and SUGAWARA, K., *Thin Solid Films*, **595** (2015) 1.

[12] MOH, G. K., VARGHESE, O. K., PAULOSE, M., SHANKAR, K. and GRIMES, C. A., *Solar Energy Mater, Solar Cells*, **90** (2006) 2011.

[13] MACAK, J. M., TSUCHIYA, H., GHICOV, G., TASUDA, K., HAHN, R., BAUER, S. and SCHMUKI, P., *Curr. Opi. Solid State Mater. Sci*., **11** (2007) 3.

[14] UCHAKER, E., ZHENG, Y. Z., LI, S., CANDELARIS, S. L., HU, S. and CAO, G. Z., *J. Mater. Chem.*, A. **2**, (2014) 18208.

[15] MUSIĆ, S., Filipović, N. and Sekovanić, Braz., L., *J. Chem. Eng*., **28** (2011) 89.

[16] ITAGAKI, M., in *Electrochemistry, Impedance method*, 2nd edition (Maruzen, Tokyo, 2014), P.93.

[17] KÖTZ, R. and CARLEN, M., *Electrochim. Acta.*, **45** (2000) 2483.

[18] CONWAY. B. E. and PELL, W. G., *J. Power Sources*, **105** (2002) 169.

[19] ITAGAKI, M. in *Electrochemistry, Impedance method*, 2nd edition (Maruzen, Tokyo, 2014), P.155.

[20] ONO, S., MACHIDA, K., ASHO, H., HASHIMOTO, H. and FUKUHARA, M., The 10th Porous Semiconductors-Science and Technology (PSST2016) Conference, Tarragona, Spain, 2015, pp.214-215.

[21] OKAMURA, M. in *Electric Double Layer Capacitor and Its Storage System*, (Nikkan Kogyo, Tokyo, 2011).

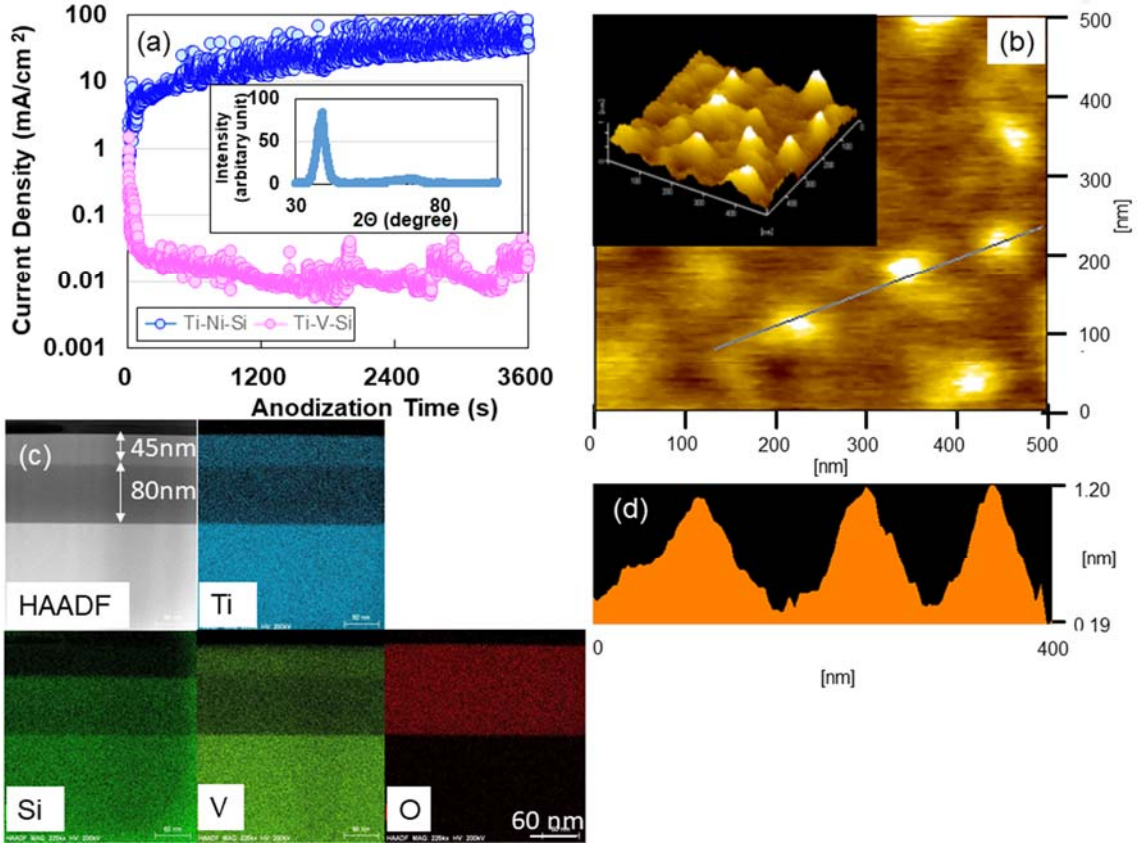

Fig. 1 (a) Current-time curves of Ti-Ni-Si and during anodization at 60V for 3,600 s in 0.4 M H_2SO_4. (b) AFM image and (d) heights measured from the valley bottom along blue line. (c) HAADF-STEM image and mapping profiles of Ti, Si, V, and O. Inset: (a) X-ray pattern for anodized specimen of Ti−V−Si amorphous alloy ribbon. (b) Three-dimensional AFM image for anodized specimen.

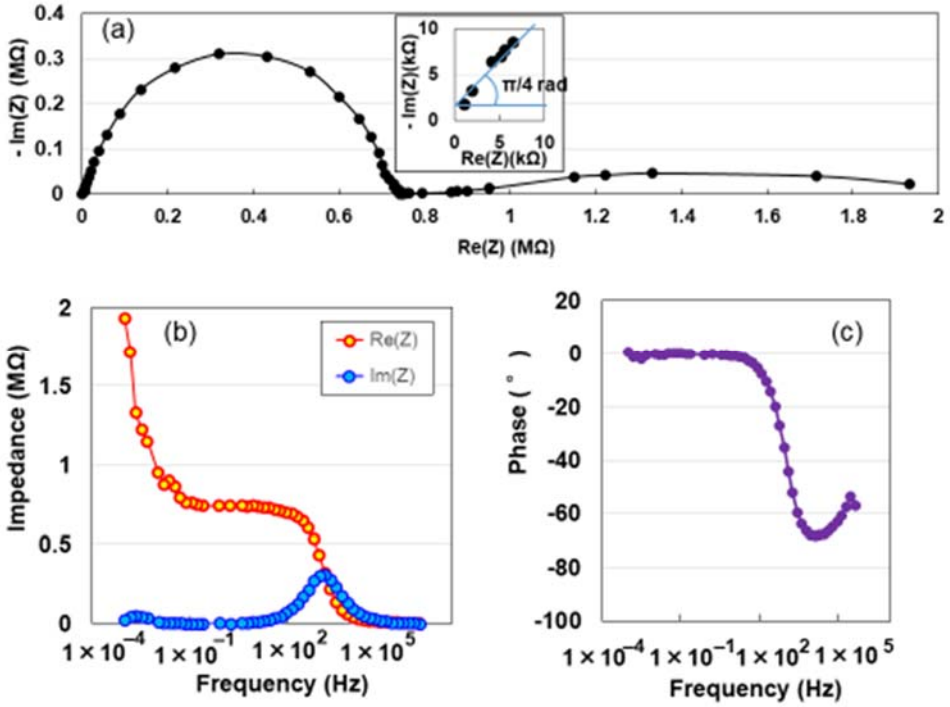

Fig. 2 Nyquist plot as a function of frequency for ATO device (a). Bode plots as a function of frequency for the real and imaginary impedances (b) and phase angle (c).

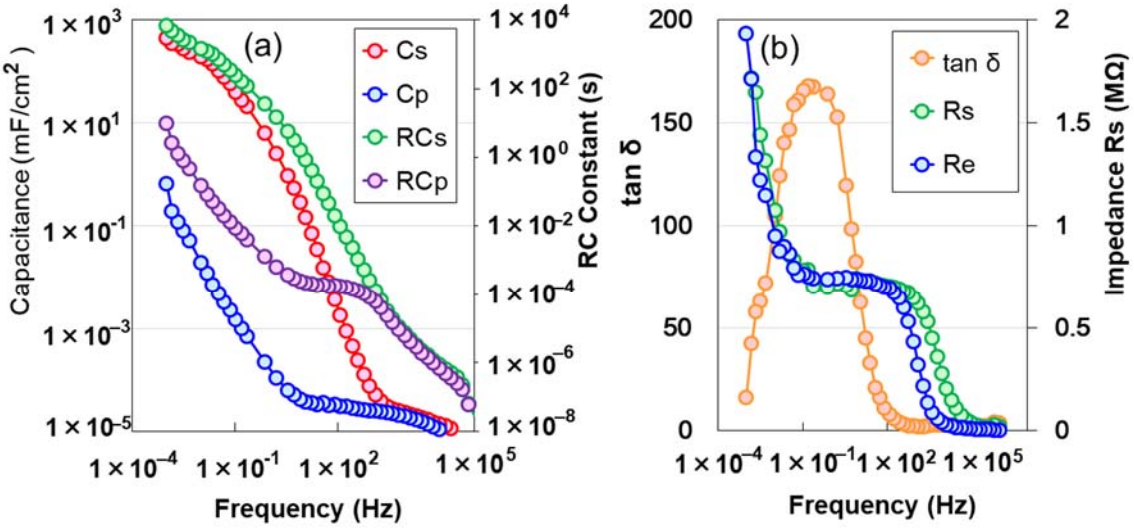

Fig. 3 Frequency dependence of series and parallel capacitances, *RC* time constant for *RCs* and *RCp* (a) and electric loss, tan δ, and series *Rs* and parallel *Re* resistances (b)

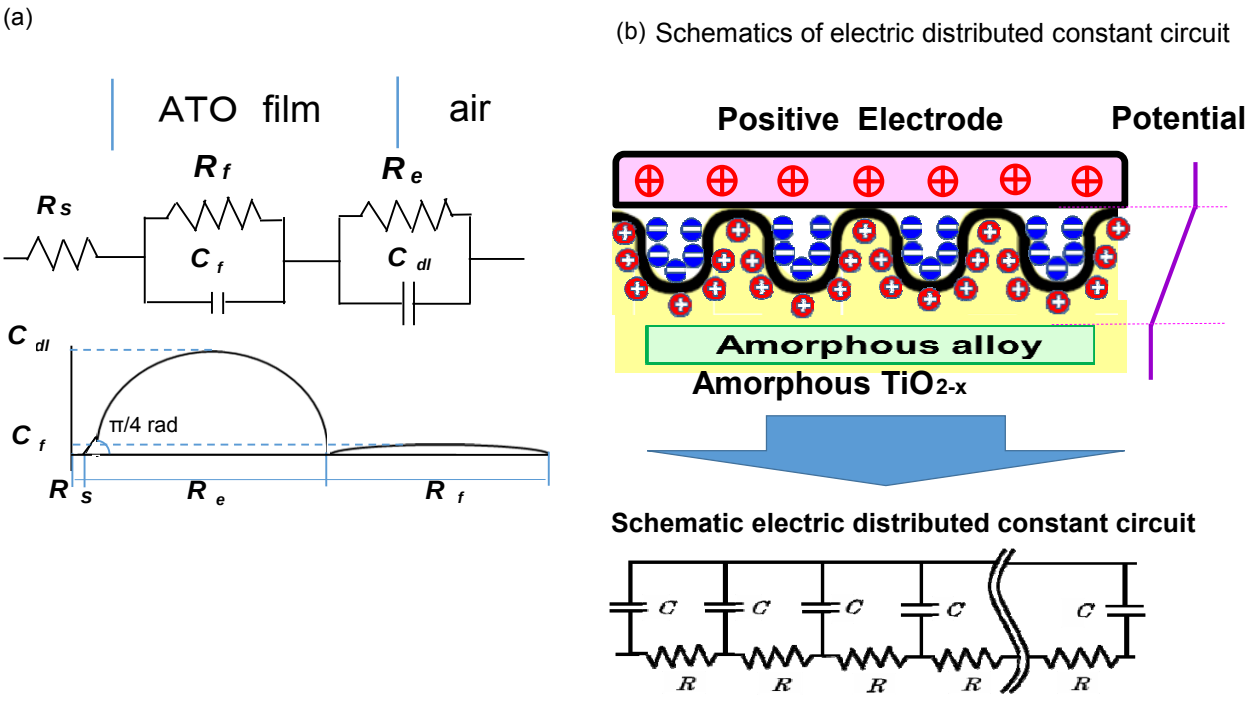

Fig. 4 Equivalent circuit (a) corresponding to Nyquist diagram in Fig. 2a. (b) Schematic representation of fabricated ATO device with an electric distributed-constant equipment circuit organizing the amorphous TiO_{2-x} surface.